Laplace-Fourier-domain dispersion analysis of an average derivative optimal scheme for scalar-wave equation

Jing-Bo Chen

Key Laboratory of Petroleum Resources Research, Institute of Geology and Geophysics, Chinese Academy of Sciences, P.O. Box 9825, Beijing 100029, China.
E-mail: chenjb@mail.igcas.ac.cn

GJI Seismology

SUMMARY

By using low-frequency components of the damped wavefield, Laplace-Fourier-domain full waveform inversion (FWI) can recover a long-wavelength velocity model from the original undamped seismic data lacking low-frequency information. Laplace-Fourier-domain modelling is an important foundation of Laplace-Fourier-domain FWI. Based on the numerical phase velocity and the numerical attenuation propagation velocity, a method for performing Laplace-Fourier-domain numerical dispersion analysis is developed in this paper. This method is applied to an average-derivative optimal scheme. The results show that within the relative error of 1 per cent, the Laplace-Fourier-domain average-derivative optimal scheme requires seven gridpoints per smallest wavelength and smallest pseudo-wavelength for both equal and unequal directional sampling intervals. In contrast, the classical five-point scheme requires 23 gridpoints per smallest wavelength and smallest pseudo-wavelength to achieve the same accuracy. Numerical experiments demonstrate the theoretical analysis.

Key words: Seismic tomography; Computational seismology; Wave propagation.

INTRODUCTION

Conventional frequency-domain full waveform inversion (FWI) methods often fail to recover long-wavelength components of the velocity model from seismic data lacking low-frequency information. To address this issue, Laplace-domain FWI was proposed (Shin & Cha 2008). Smoother objective function and insensitivity to the lack of low-frequency information in Laplace domain leads to the success of Laplace-domain FWI (Ha & Shin 2012). Combined with conventional FWI, Laplace-domain FWI has been successfully applied to real data (Shin *et al.* 2010; Ha *et al.* 2012).

Shin & Cha (2009) further introduced Laplace-Fourier-domain FWI which is equivalent to the complex-frequency-domain method used by Brenders & Pratt (2007). Instead of using only the zero frequency component of the damped wavefield in Laplace-domain FWI, Laplace-Fourier-domain FWI uses the low-frequency components of the damped wavefield. Moreover, using full-frequency components of the damped wavefield leads to full Laplace-Fourier-domain FWI (Shin *et al.* 2010). Forward modelling in Laplace–Fourier domain is an important part of Laplace-Fourier-domain FWI. In general, numerical modelling schemes for frequency-domain modelling can be directly adapted to that for Laplace-Fourier-domain modelling. For example, the average-derivative optimal scheme in Chen (2012) can be directly employed to perform Laplace-Fourier-domain modelling by simply replacing

the original frequency with the complex frequency. However, the dispersion analysis of the Laplace-Fourier-domain schemes is more complicated. Um *et al.* (2012) performed Laplace-Fourier-domain dispersion analysis by numerical experiments. Here, I will discuss theoretical dispersion analysis by the von Neumann method.

For Fourier-domain (also known as frequency-domain) dispersion analysis, one uses the numerical phase velocity which depends on the number of gridpoints per wavelength (Jo *et al.* 1996; Chen 2012). For Laplace-domain dispersion analysis, one uses the numerical attenuation propagation velocity which depends on the number of gridpoints per pseudo-wavelength (Chen 2014). When it comes to Laplace-Fourier-domain dispersion analysis, both the numerical phase velocity and the numerical attenuation propagation velocity are involved. More significantly, the numerical phase velocity depends on both the number of gridpoints per wavelength and the number of gridpoints per pseudo-wavelength, and the same is true for the numerical attenuation propagation velocity. This is why the dispersion analysis of the Laplace-Fourier-domain schemes becomes more complicated.

In the next section, I will present the Laplace-Fourier-domain average-derivative optimal scheme. This is followed by the optimization of coefficients and a numerical dispersion analysis. Numerical examples are then presented to demonstrate the theoretical analysis.

A LAPLACE-FOURIER-DOMAIN SCHEME

Consider the 2-D scalar-wave equation in the Laplace–Fourier domain

$$\frac{\partial^2 P}{\partial x^2} + \frac{\partial^2 P}{\partial z^2} + \frac{(\omega + \mathrm{i}\,s)^2}{v^2} P = 0, \qquad (1)$$

where P is the pressure wavefield, ω is the angular frequency, s is the Laplace damping constant, $\mathrm{i} = \sqrt{-1}$ and $v(x, z)$ is the velocity. Here we assume constant density. Generalization to the variable density case can be easily done (Chen 2012).

Numerical schemes for eq. (1) can be directly obtained from the corresponding frequency-domain schemes. Frequency-domain schemes include the classical five-point scheme (Pratt & Worthington 1990), the optimal nine-point scheme for equal directional sampling intervals (Jo *et al.* 1996), the average-derivative optimal scheme (Chen 2012) and the directional-derivative optimal scheme (Chen 2013).

In this paper, I consider an average-derivative nine-point scheme for eq. (1):

$$\frac{\bar{P}_{m+1, n} - 2\bar{P}_{m, n} + \bar{P}_{m-1, n}}{\Delta x^2} + \frac{\tilde{P}_{m, n+1} - 2\tilde{P}_{m, n} + \tilde{P}_{m, n-1}}{\Delta z^2}$$

$$+ \frac{(\omega + \mathrm{i}\,s)^2}{v_{m, n}^2} (c P_{m, n} + d(P_{m+1, n} + P_{m-1, n} + P_{m, n+1} + P_{m, n-1})$$

$$+ f\,(P_{m+1, n+1} + P_{m-1, n+1} + P_{m+1, n-1} + P_{m-1, n-1})) = 0, \qquad (2)$$

where

$$\bar{P}_{m+1, n} = \frac{1 - \alpha}{2} P_{m+1, n+1} + \alpha P_{m+1, n} + \frac{1 - \alpha}{2} P_{m+1, n-1},$$

$$\bar{P}_{m, n} = \frac{1 - \alpha}{2} P_{m, n+1} + \alpha P_{m, n} + \frac{1 - \alpha}{2} P_{m, n-1},$$

$$\bar{P}_{m-1, n} = \frac{1 - \alpha}{2} P_{m-1, n+1} + \alpha P_{m-1, n} + \frac{1 - \alpha}{2} P_{m-1, n-1},$$

and

$$\tilde{P}_{m, n+1} = \frac{1 - \beta}{2} P_{m+1, n+1} + \beta P_{m, n+1} + \frac{1 - \beta}{2} P_{m-1, n+1},$$

$$\tilde{P}_{m, n} = \frac{1 - \beta}{2} P_{m+1, n} + \beta P_{m, n} + \frac{1 - \beta}{2} P_{m-1, n},$$

$$\tilde{P}_{m, n-1} = \frac{1 - \beta}{2} P_{m+1, n-1} + \beta P_{m, n-1} + \frac{1 - \beta}{2} P_{m-1, n-1},$$

where $P_{m, n} \approx P(m\Delta x, n\Delta z)$; $v_{n, m} \approx v(m\Delta x, n\Delta z)$; Δx and Δz are directional sampling intervals; α, β, c and d are weighted coefficients which should be optimized; and $f = \frac{1 - c - 4d}{4}$.

The average-derivative nine-point scheme (2) includes the classical five-point scheme as a special case, because when $\alpha = 1$, $\beta = 1$, $c = 1$ and $d = 0$, the scheme (2) becomes

$$\frac{P_{m+1, n} - 2P_{m, n} + P_{m-1, n}}{\Delta x^2} + \frac{P_{m, n+1} - 2P_{m, n} + P_{m, n-1}}{\Delta z^2}$$

$$+ \frac{(\omega + \mathrm{i}\,s)^2}{v_{m, n}^2} P_{m, n} = 0. \qquad (3)$$

OPTIMIZATION AND DISPERSION ANALYSIS

Consider an attenuating plane-wave function in the following form:

$$P(k, \boldsymbol{r}) = P_0 \mathrm{e}^{\mathrm{i}kr}, \qquad (4)$$

where $\boldsymbol{r} = \sin(\theta)x + \cos(\theta)z$, $k = k_r + \mathrm{i}\,k_i$, P_0 is a constant and θ is the propagation angle. Here $k_r = \frac{\omega}{v}$ is the wavenumber, and $k_i = \frac{s}{v}$ is the pseudo-wavenumber (Chen 2014).

Substituting eq. (4) into eq. (2) and assuming a constant v, one obtains the discrete dispersion relation

$$\frac{(\omega + \mathrm{i}\,s)^2}{v^2} = \frac{A}{B\,\Delta x^2}, \qquad (5)$$

where

$$A = \left[(1 - \alpha) \cos\left(\frac{k\Delta x}{R} \cos(\theta) \right) + \alpha \right] [2 - 2\cos(k\Delta x \sin(\theta))]$$

$$+ R^2 \left[(1 - \beta) \cos(k\Delta x \sin(\theta)) + \beta \right]$$

$$\times \left[2 - 2\cos\left(\frac{k\Delta x}{R} \cos(\theta) \right) \right],$$

$$B = c + 2d \left[\cos\left(\frac{k\Delta x}{R} \cos(\theta) \right) + \cos(k\Delta x \sin(\theta)) \right]$$

$$+ 4f \cos\left(\frac{k\Delta x}{R} \cos(\theta) \right) \cos(k\Delta x \sin(\theta)),$$

where $R = \frac{\Delta x}{\Delta z}$.

One can express $k\Delta x$ as

$$k\Delta x = k_r \Delta x + \mathrm{i}\,k_i \Delta x = \frac{2\pi}{G_r} + \mathrm{i}\,\frac{2\pi}{G_i}, \qquad (6)$$

where $G_r = \frac{2\pi}{k_r \Delta x}$ is the number of gridpoints per wavelength, and $G_i = \frac{2\pi}{k_i \Delta x}$ is the number of gridpoints per pseudo-wavelength. Here, I first consider the case $\Delta x \geq \Delta z$.

Set

$$\mathcal{F}(G_r, G_i, \theta) = \mathcal{F}_r(G_r, G_i, \theta) + \mathrm{i}\mathcal{F}_i(G_r, G_i, \theta) = \sqrt{\frac{A}{B}}. \qquad (7)$$

where $\mathcal{F}_r(G_r, G_i, \theta)$ and $\mathcal{F}_i(G_r, G_i, \theta)$ are the real and imaginary parts of $\mathcal{F}(G_r, G_i, \theta)$, respectively. Here $\sqrt{\frac{A}{B}}$ denotes the square root of $\frac{A}{B}$ whose angle φ satisfying $-\frac{\pi}{2} < \varphi \leq \frac{\pi}{2}$.

From eqs (5) and (7), one can obtain

$$\frac{\omega}{v} = \frac{1}{\Delta x} \mathcal{F}_r(G_r, G_i, \theta), \qquad (8)$$

$$\frac{s}{v} = \frac{1}{\Delta x} \mathcal{F}_i(G_r, G_i, \theta). \qquad (9)$$

From eqs (8) and (9), normalized numerical phase velocity and numerical attenuation propagation velocity can be obtained as follows:

$$\frac{v_r}{v} = \frac{G_r}{2\pi} \mathcal{F}_r(G_r, G_i, \theta), \qquad (10)$$

$$\frac{v_i}{v} = \frac{G_i}{2\pi} \mathcal{F}_i(G_r, G_i, \theta), \qquad (11)$$

where $v_r = \frac{\omega}{k_r}$ and $v_i = \frac{s}{k_i}$. Note that $\frac{v_r}{v}$ depends on both G_r and G_i. The same is true for $\frac{v_i}{v}$.

Table 1. Optimization coefficients for α, β, c and d for different $\frac{\Delta x}{\Delta z}$ when $\Delta x \geq \Delta z$.

	α	β	c	d
$\frac{\Delta x}{\Delta z} = 1$	0.833220	0.833234	0.666603	0.083349
$\frac{\Delta x}{\Delta z} = 1.5$	0.465714	0.996631	0.666632	0.083342
$\frac{\Delta x}{\Delta z} = 2$	0.171721	0.998697	0.666656	0.083336
$\frac{\Delta x}{\Delta z} = 2.5$	0.058736	0.957257	0.666673	0.083332
$\frac{\Delta x}{\Delta z} = 3$	0.059368	0.919334	0.666683	0.083329
$\frac{\Delta x}{\Delta z} = 3.5$	0.061366	0.896366	0.666692	0.083327
$\frac{\Delta x}{\Delta z} = 4$	0.063906	0.881444	0.666698	0.083326

Table 2. Optimization coefficients for α, β, c and d for different $\frac{\Delta z}{\Delta x}$ when $\Delta x < \Delta z$.

	α	β	c	d
$\frac{\Delta z}{\Delta x} = 1.5$	0.996631	0.465714	0.666632	0.083342
$\frac{\Delta z}{\Delta x} = 2$	0.998697	0.171721	0.666656	0.083336
$\frac{\Delta z}{\Delta x} = 2.5$	0.957257	0.058736	0.666673	0.083332
$\frac{\Delta z}{\Delta x} = 3$	0.919334	0.059368	0.666683	0.083329
$\frac{\Delta z}{\Delta x} = 3.5$	0.896366	0.061366	0.666692	0.083327
$\frac{\Delta z}{\Delta x} = 4$	0.881444	0.063906	0.666698	0.083326

When $\Delta x \neq \Delta z$, the quantity G_i and G_r are defined with respect to the larger sampling interval. That is why I separate the analysis for $\Delta x \geq \Delta z$ and $\Delta z > \Delta x$.

The coefficients α, β, c and d are determined by minimizing the velocity error:

$$E(\alpha, \beta, c, d) = \iiint \left[\left(1 - \frac{v_r(\theta, \tilde{k}_r, \tilde{k}_i; \alpha, \beta, c, d)}{v} \right)^2 \right.$$
$$\left. + \left(1 - \frac{v_i(\theta, \tilde{k}_r, \tilde{k}_i; \alpha, \beta, c, d)}{v} \right)^2 \right] d\tilde{k}_r \, d\tilde{k}_i \, d\theta, \tag{12}$$

where $\tilde{k}_r = \frac{1}{G_r}$ and $\tilde{k}_i = \frac{1}{G_i}$.

The ranges of $\tilde{k}_r$, $\tilde{k}_i$ and θ are taken as [0, 0.15], [0, 0.15] and $[0, \frac{\pi}{2}]$, respectively. I use a constrained non-linear optimization program fmincon in Matlab to determine the optimization coefficients. The optimization coefficients for different $R = \frac{\Delta x}{\Delta z}$ are listed in Table 1. The coefficients are different from their counterparts of Fourier-domain and Laplace-domain average-derivative optimal schemes (Chen 2012, 2014). This is because numerical dispersion analysis of Laplace–Fourier domain is fundamentally different from that of Laplace domain or Fourier domain. For Laplace-Fourier-domain analysis, both numerical attenuation propagation velocity and numerical phase velocity are involved. To reach the required accuracy, one must reduce the errors of these two velocities simultaneously. This leads to different optimization coefficients and more gridpoints per wavelength. As long as $s \neq 0$ and $\omega \neq 0$, the result of Laplace-Fourier-domain dispersion analysis is independent of the values of s and ω. The reason is that the dispersion analysis is based on pseudo-wavelength and wavelength which cannot be determined by the values of s and ω alone.

If $\Delta z > \Delta x$, one obtains the discrete dispersion relation

$$\frac{(\omega + \mathrm{i}\, s)^2}{v^2} = \frac{A_1}{B_1 \Delta x^2}, \tag{13}$$

where

$$A_1 = R^2 \left[(1 - \alpha) \cos(k\Delta z \cos(\theta)) + \alpha \right] \left[2 - 2\cos\left(\frac{k\Delta z}{R} \sin(\theta) \right) \right]$$
$$+ \left[(1 - \beta) \cos\left(\frac{k\Delta z}{R} \sin(\theta) \right) + \beta \right] \left[2 - 2\cos(k\Delta z \cos(\theta)) \right],$$

$$B_1 = c + 2d \left[\cos(k\Delta z \cos(\theta)) + \cos\left(\frac{k\Delta z}{R} \sin(\theta) \right) \right]$$
$$+ 4f \cos(k\Delta z \cos(\theta)) \cos\left(\frac{k\Delta z}{R} \sin(\theta) \right),$$

where $R = \frac{\Delta z}{\Delta x}$.

One can express $k\Delta z$ as

$$k\Delta z = k_r \Delta z + \mathrm{i}\, k_i \Delta z = \frac{2\pi}{G_r} + \mathrm{i}\, \frac{2\pi}{G_i}, \tag{14}$$

where $G_r = \frac{2\pi}{k_r \Delta z}$ is the number of gridpoints per wavelength, and $G_i = \frac{2\pi}{k_i \Delta z}$ is the number of gridpoints per pseudo-wavelength.

The optimization coefficients for the case of $\Delta z > \Delta x$ are listed in Table 2. Compared to the case of $\Delta x \geq \Delta z$, the only change is that the coefficients α and β are exchanged. This is because only the roles of x and z are exchanged in this case.

Now I perform numerical dispersion analysis. Fig. 1 shows normalized numerical phase velocity curves $\frac{v_r}{v}$ of the five-point scheme (3) and the average-derivative optimal nine-point scheme (2) for different propagation angles when $\frac{\Delta x}{\Delta z} = 1$. In each plot, $\frac{1}{G_r}$ varies, and $\frac{1}{G_i}$ is fixed. For the five-point scheme (3), the normalized numerical phase velocity errors increase with increasing $\frac{1}{G_r}$ for small fixed values of $\frac{1}{G_i}$, and for large fixed values of $\frac{1}{G_i}$, the normalized numerical phase velocity errors decrease with increasing $\frac{1}{G_r}$. This phenomenon indicates that the normalized numerical phase velocity errors depend on both $\frac{1}{G_r}$ and $\frac{1}{G_i}$. For the average-derivative optimal nine-point scheme (2), the normalized numerical phase velocity errors remain within 1 per cent. Fig. 2 shows normalized numerical phase velocity surfaces $\frac{v_r}{v}$ of the five-point scheme (3) and the average-derivative optimal nine-point sc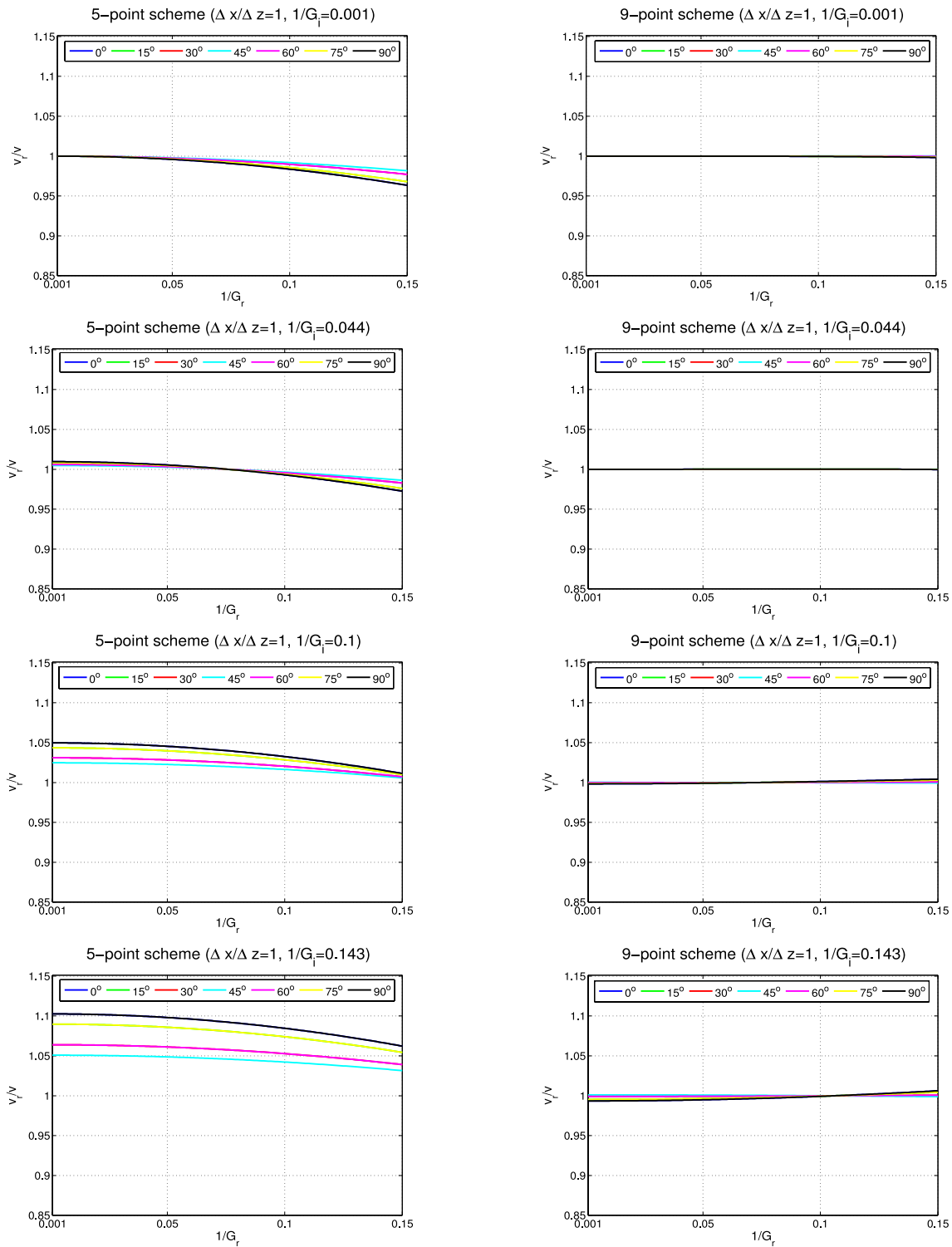heme (2) for different propagation angles when $\frac{\Delta x}{\Delta z} = 1$. In each plot, both $\frac{1}{G_r}$ and $\frac{1}{G_i}$ vary. These plots provide more complete delineation of the normalized numerical phase velocity $\frac{v_r}{v}$. For the five-point scheme (3), large errors occur whenever $\frac{1}{G_r}$ or $\frac{1}{G_i}$ is large. For the average-derivative optimal nine-point scheme (2), the errors remain within 1 per cent for the whole range of $\frac{1}{G_r}$ and $\frac{1}{G_i}$.

Fig. 3 shows normalized numerical attenuation propagation velocity curves $\frac{v_i}{v}$ of the five-point scheme (3) and the average-derivative optimal nine-point scheme (2) for different propagation angles when $\frac{\Delta x}{\Delta z} = 1$. In each plot, $\frac{1}{G_i}$ varies, and $\frac{1}{G_r}$ is fixed. For the five-point scheme (3), the normalized numerical attenuation propagation velocity errors increase with increasing $\frac{1}{G_i}$ for small fixed values of $\frac{1}{G_r}$, and for large fixed values of $\frac{1}{G_r}$, the normalized numerical attenuation propagation velocity errors decrease with increasing $\frac{1}{G_r}$. However, unlike the case of normalized numerical phase velocity errors, the normalized numerical attenuation propagation velocity errors have the opposite sign. For the average-derivative optimal nine-point scheme (2), the normalized numerical attenuation propagation velocity errors remain within 1 per cent. Fig. 4 shows normalized numerical attenuation propagation velocity surfaces $\frac{v_i}{v}$ of the five-point scheme (3) and the average-derivative optimal nine-point scheme (2) for different propagation angles when
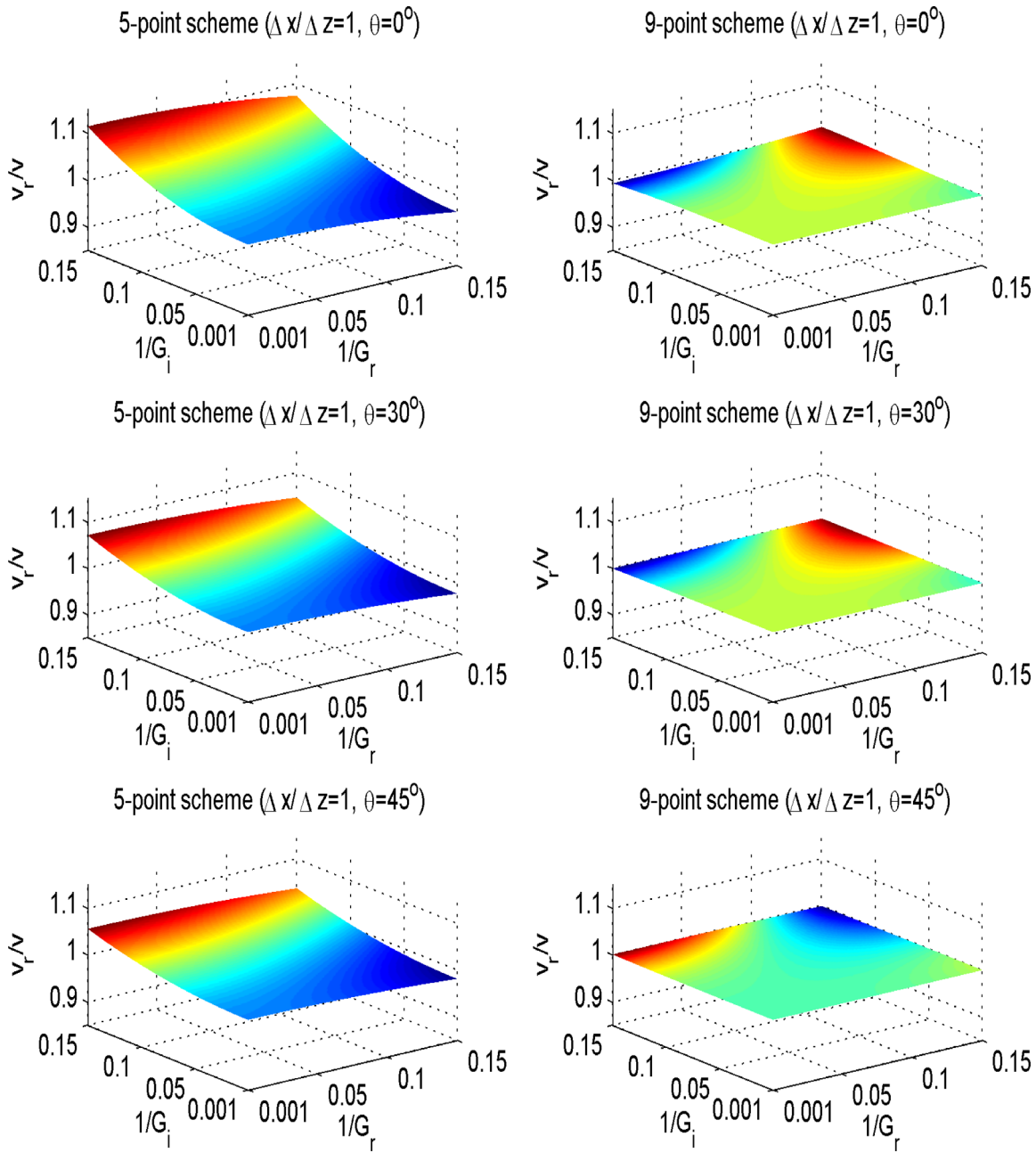
Figure 1. Normalized numerical phase velocity curves $\frac{v_r}{v}$ of the five-point scheme (3) and the average-derivative optimal nine-point scheme (2) for different propagation angles. In each plot, $\frac{1}{G_r}$ varies and $\frac{1}{G_i}$ is fixed. Here $\frac{\Delta x}{\Delta z} = 1$.

$\frac{\Delta x}{\Delta z} = 1$. In each plot, both $\frac{1}{G_r}$ and $\frac{1}{G_i}$ vary. Again, these plots provide more complete delineation of the normalized numerical attenuation propagation velocity $\frac{v_i}{v}$. For the five-point scheme (3), large errors occur whenever $\frac{1}{G_r}$ or $\frac{1}{G_i}$ is large. For the average-derivative optimal

nine-point scheme (2), the errors remain within 1 per cent for the whole range of $\frac{1}{G_r}$ and $\frac{1}{G_i}$.

From Figs 1–4, one can draw a conclusion: within the error of 1 per cent, the five-point scheme (3) requires 23 gridpoints per

Figure 2. Normalized numerical phase velocity surfaces $\frac{v_r}{v}$ of the five-point scheme (3) and the average-derivative optimal nine-point scheme (2) for different propagation angles. In each plot, both $\frac{1}{G_r}$ and $\frac{1}{G_i}$ vary. Here $\frac{\Delta x}{\Delta z} = 1$.

shortest wavelength and shortest pseudo-wavelength. In contrast, the average-derivative optimal nine-point scheme (2) requires seven gridpoints per shortest wavelength and shortest pseudo-wavelength. Figs 5–8 show the corresponding results for the case of $\frac{\Delta x}{\Delta z} = 2$. In this case, the same conclusion can be drawn with respect to the number of gridpoints per shortest wavelength and shortest pseudo-wavelength.

NUMERICAL EXAMPLES

In this section, I present numerical examples to verify the theoretical analysis on the average-derivative optimal nine-point scheme (2) and the classical five-point scheme (3).

Consider a homogeneous velocity model with a velocity of $2100 \, \mathrm{m \, s^{-1}}$. Horizontal and vertical distances are both 6 km (Fig. 9). The angular frequency ω and the Laplace damping constant s are both taken to be $10 \, \pi \, \mathrm{s^{-1}}$. Accordingly, the wavelength and the pseudo-wavelength are both $2100/(10\pi/2\pi) \, \mathrm{m} = 420 \, \mathrm{m}$. According to the criterion of seven gridpoints per smallest wavelength and smallest pseudo-wavelength, horizontal sampling interval is determined by $\Delta x = 420/7 \, \mathrm{m} = 60 \, \mathrm{m}$. Vertical sampling interval is taken as $\Delta z = \Delta x = 60 \, \mathrm{m}$. For this ratio of directional sampling intervals, the optimization coefficients of the scheme (2) are $\alpha = 0.833220$, $\beta = 0.833234$, $c = 0.666603$ and $d = 0.083349$ (Table 1). Horizontal and vertical samplings are $nx = 101$ and $nz = 101$, respectively. A Ricker wavelet is placed at the centre of
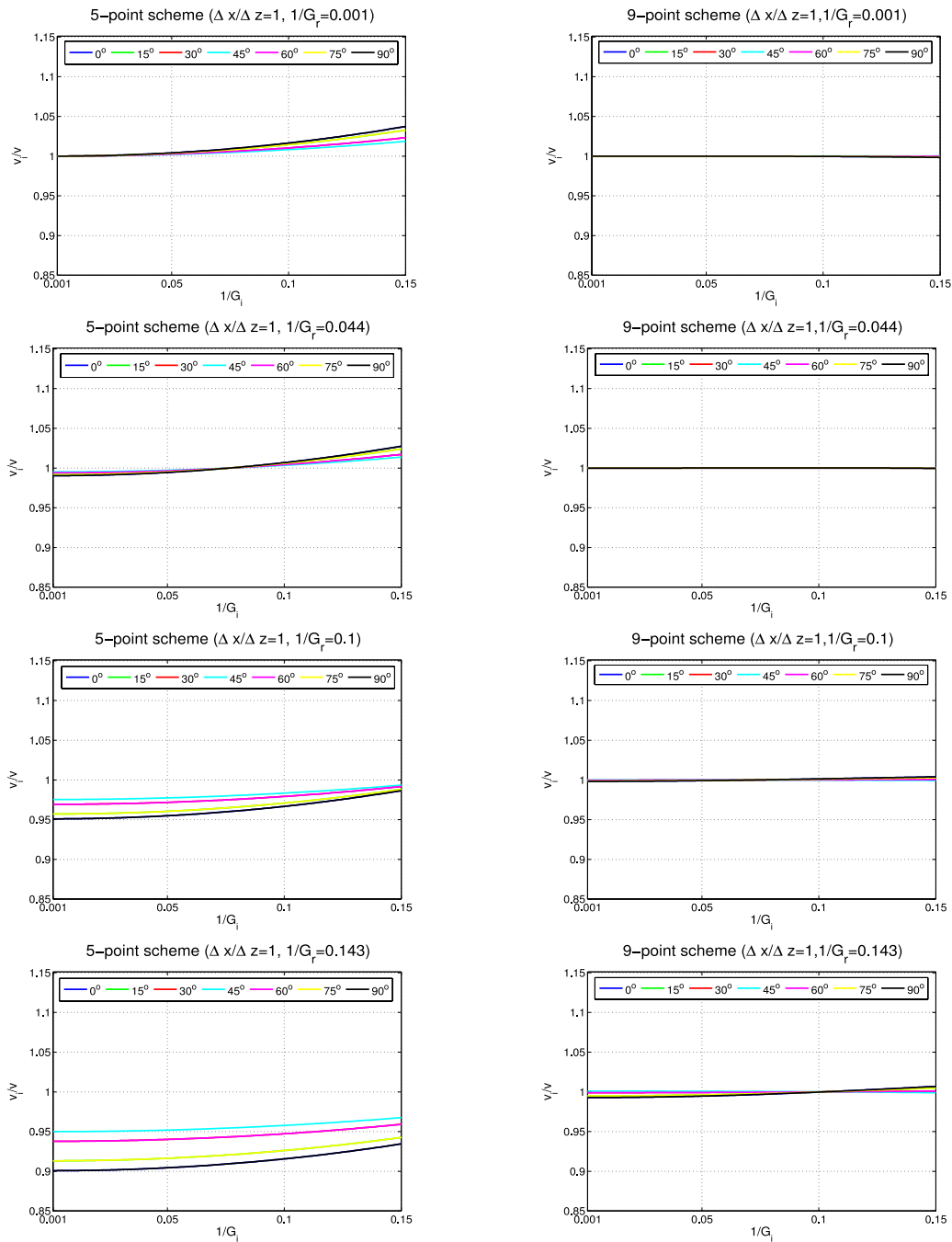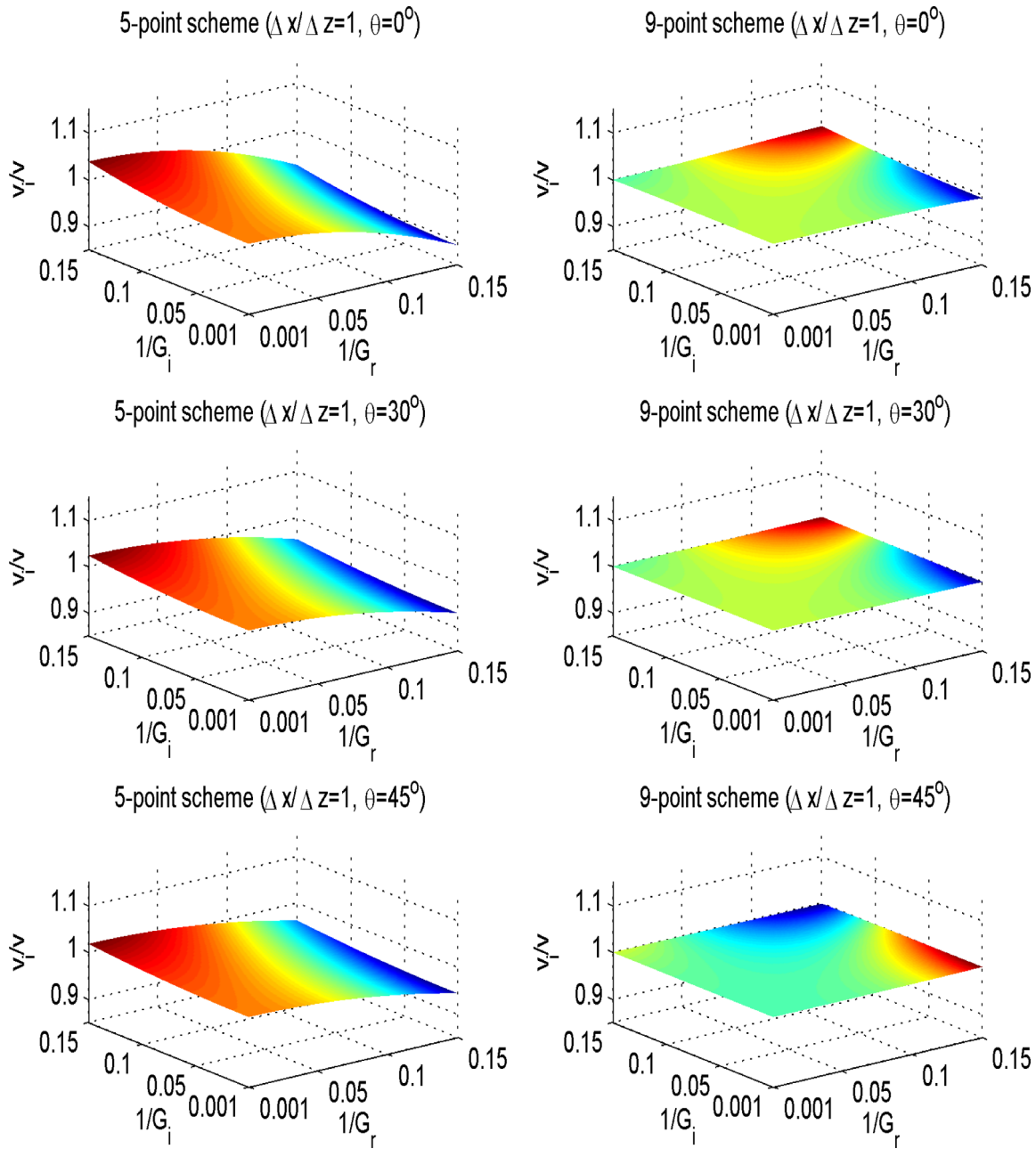
Figure 3. Normalized numerical attenuation propagation velocity curves $\frac{v_i}{v}$ of the five-point scheme (3) and the average-derivative optimal nine-point scheme (2) for different propagation angles. In each plot, $\frac{1}{G_i}$ varies and $\frac{1}{G_r}$ is fixed. Here $\frac{\Delta x}{\Delta z} = 1$.

the model as a source, and a receiver array is placed at a depth of 1.5 km.

For the analytical solution, the following formula is used (Alford *et al.* 1974):

$$P(x, z, \omega, s) = i\pi H_0^{(2)} \left(\frac{\omega - is}{v} r \right) F(\omega, s), \qquad (15)$$

where i is the imaginary unit, $H_0^{(2)}$ is the second Hankel function of order zero, $F(\omega, s)$ is the Laplace–Fourier transform of the Ricker

wavelet and $r = \sqrt{(x - x_0)^2 + (z - z_0)^2}$. Here (x_0, z_0) is the source position.

Fig. 10 shows the Laplace-Fourier-domain seismograms (real part) computed with the analytical formula (15), the classical five-point scheme (3) and the average-derivative optimal nine-point scheme (2). The simulation result with the average-derivative optimal nine-point scheme (2) is in good agreement with the analytical result. The result with the classical five-point scheme (3) exhibits large errors due to numerical dispersion. To further demonstrate the

Figure 4. Normalized numerical attenuation propagation velocity surfaces $\frac{v_i}{v}$ of the five-point scheme (3) and the average-derivative optimal nine-point scheme (2) for different propagation angles. In each plot, both $\frac{1}{G_i}$ and $\frac{1}{G_r}$ vary. Here $\frac{\Delta x}{\Delta z} = 1$.

result of dispersion analysis, Fig. 11 displays the Laplace-Fourier-domain seismograms computed with the analytical formula (15), the average-derivative optimal nine-point scheme (3) with seven gridpoints per wavelength and pseudo-wavelength, and the average-derivative optimal nine-point scheme (3) with five gridpoints per wavelength and pseudo-wavelength. One can see that the result obtained with the average-derivative optimal nine-point scheme (3) with five gridpoints per wavelength and pseudo-wavelength exhibits errors due to fewer gridpoints than that required by the theoretical dispersion analysis.

Now consider another case where $\Delta x \neq \Delta z$. Let $\Delta z = \Delta x/2$. Accordingly, vertical samplings become $nz = 201$. For this ra-

tio of directional sampling intervals, the optimization coefficients of the scheme (2) are $\alpha = 0.171721$, $\beta = 0.998697$, $c = 0.666656$ and $d = 0.083336$ (Table 1). Fig. 12 shows the Laplace-Fourier-domain seismograms computed with the analytical formula (15), the classical five-point scheme (3) and the average-derivative optimal nine-point scheme (2). The simulation result with the average-derivative optimal nine-point scheme (2) is again in good agreement with the analytical result. The result with the classical five-point scheme (3) exhibits errors due to numerical dispersion. Compared to the case where $\Delta x = \Delta z$, the errors are reduced due to the smaller Δz. These results are in line with the theoretical analysis on numerical dispersion of the
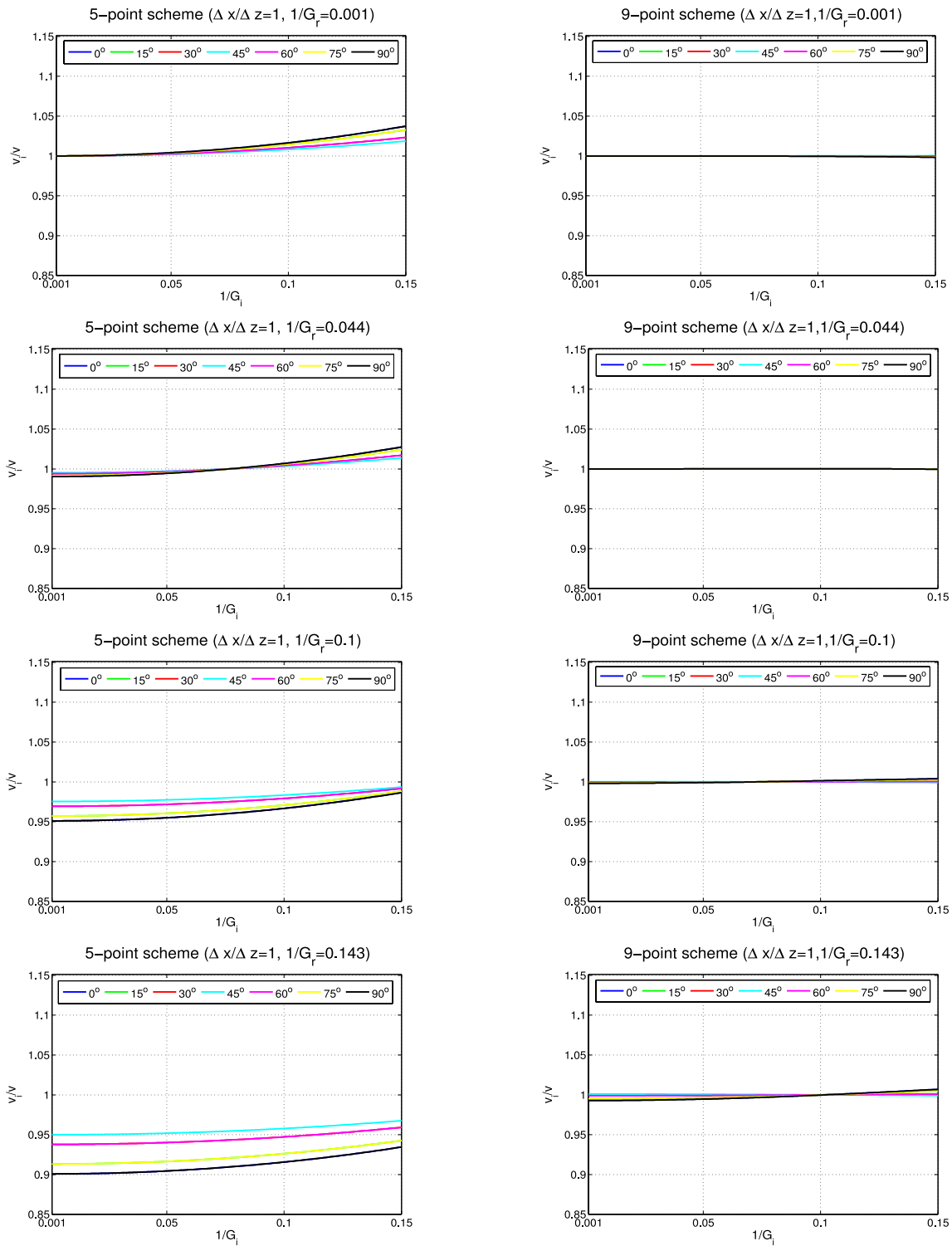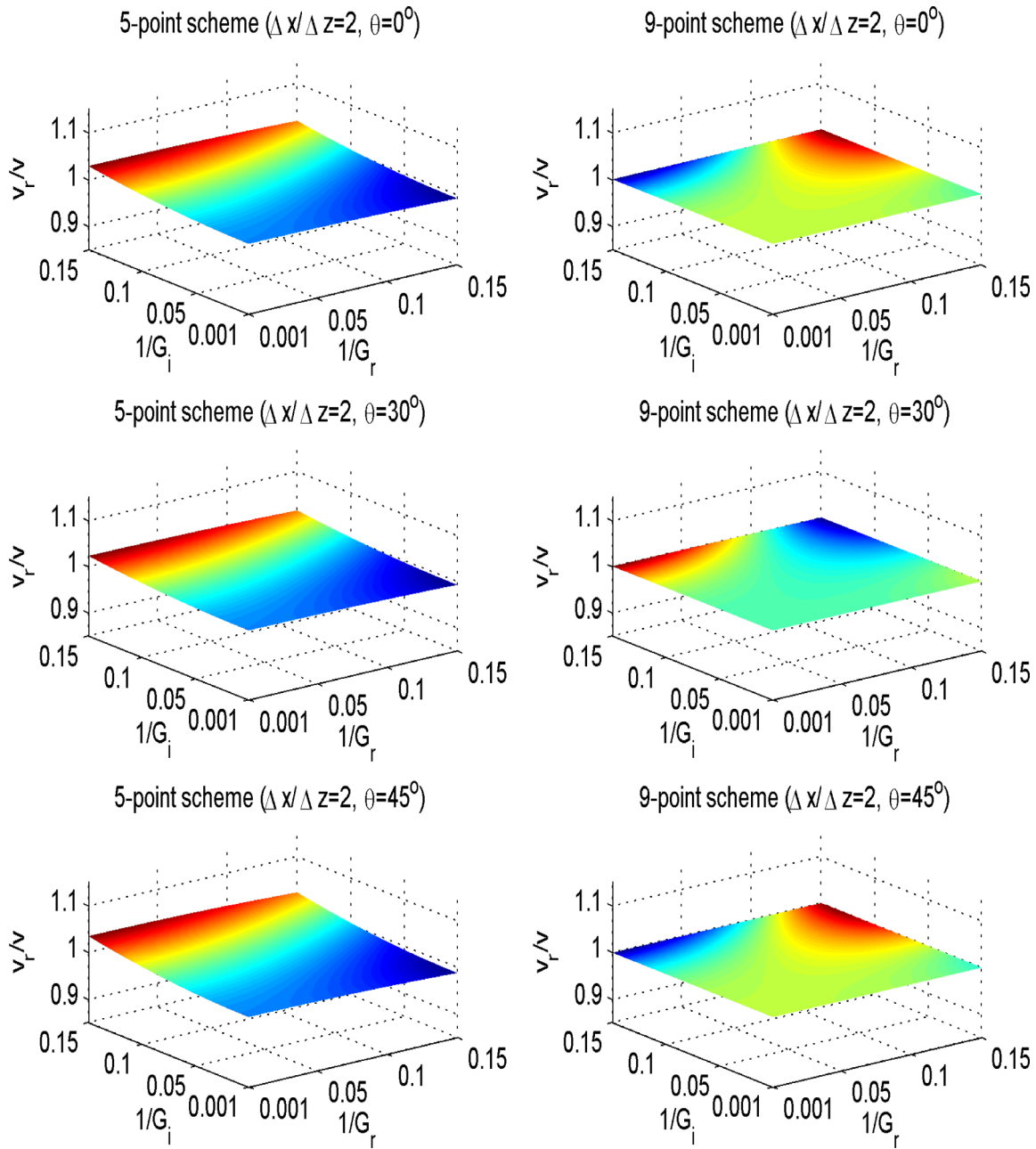
Figure 5. Normalized numerical phase velocity curves $\frac{v_r}{v}$ of the five-point scheme (3) and the average-derivative optimal nine-point scheme (2) for different propagation angles. In each plot, $\frac{1}{G_r}$ varies and $\frac{1}{G_i}$ is fixed. Here $\frac{\Delta x}{\Delta z} = 2$.

average-derivative optimal nine-point scheme (2) and the classical five-point scheme (3).

Finally, I consider a more realistic model. Fig. 13(a) shows a salt model which is a 2-D section of the SEG/EAGE salt model.

The sampling intervals are $\Delta x = 40$ m and $\Delta z = 20$ m. Horizontal and vertical samplings are $nx = 251$ and $nz = 201$, respectively. A Ricker wavelet is placed at ($x = 5$ km, $z = 2$ km) as a source, and the receivers are set at the depth of 20 m with a spacing of 40 m.

Figure 6. Normalized numerical phase velocity surfaces $\frac{v_r}{v}$ of the five-point scheme (3) and the average-derivative optimal nine-point scheme (2) for different propagation angles. In each plot, both $\frac{1}{G_r}$ and $\frac{1}{G_i}$ vary. Here $\frac{\Delta x}{\Delta z} = 2$.

Again, the angular frequency ω and the Laplace damping constant s are both taken to be $10\,\pi\ \mathrm{s}^{-1}$. Fig. 13(b) shows the Laplace-Fourier-domain seismograms computed with the classical five-point scheme (3) and the average-derivative optimal nine-point scheme (2). Since the analytical result is not available in this case, I also show the result computed by the classical five-point scheme (3) with smaller Δx and Δz for comparison. One can see that the result of the classical five-point scheme (3) with smaller spacings is closer to the result of the average-derivative optimal nine-point scheme (2). This demonstrates the greater accuracy of the average-derivative optimal nine-point scheme (2) for this salt model.

CONCLUSIONS

Based on the numerical phase velocity and the numerical attenuation propagation velocity, a Laplace-Fourier-domain method of numerical dispersion analysis is developed and applied to an average-derivative optimal nine-point scheme in Laplace–Fourier domain. The resulting optimization coefficients are different from their frequency-domain and Laplace-domain counterparts. Compared to the classical five-point scheme, this Laplace-Fourier-domain average-derivative optimal nine-point scheme reduces the number of gridpoints per shortest wavelength and shortest
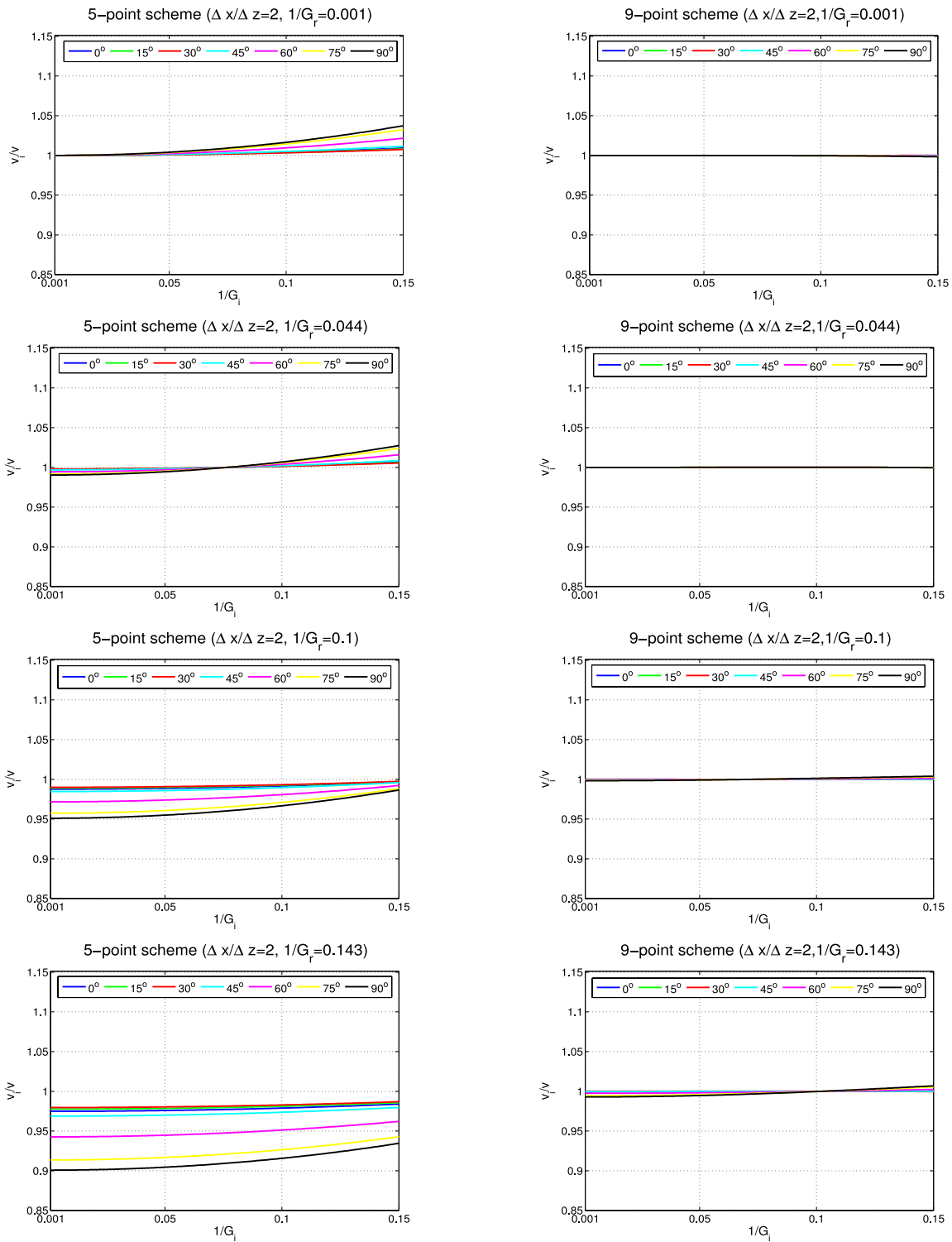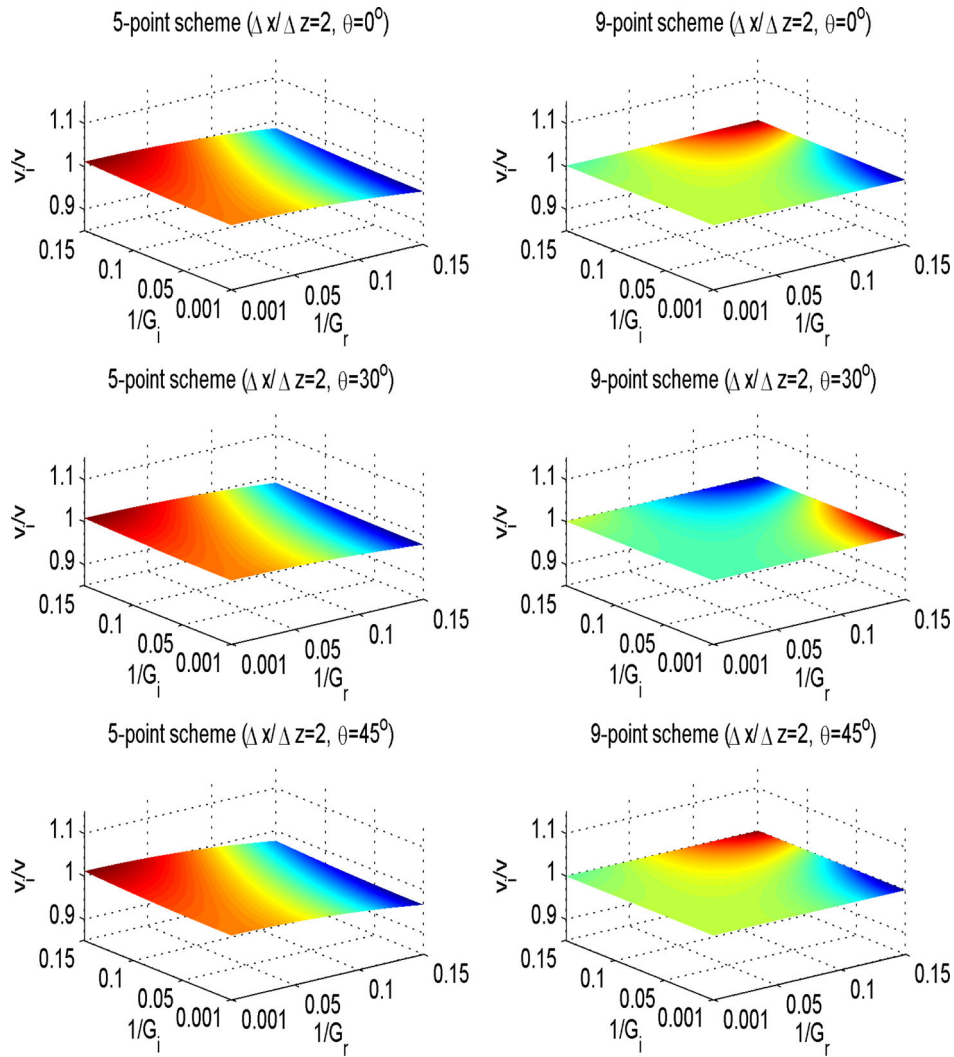
Figure 7. Normalized numerical attenuation propagation velocity curves $\frac{v_i}{v}$ of the five-point scheme (3) and the average-derivative optimal nine-point scheme (2) for different propagation angles. In each plot, $\frac{1}{G_i}$ varies and $\frac{1}{G_r}$ is fixed. Here $\frac{\Delta x}{\Delta z} = 2$.

pseudo-wavelength from 23 to 7 for both equal and unequal directional sampling intervals. Comparisons with the analytical solution for a homogenous model demonstrate the theoretical analysis.

ACKNOWLEDGEMENTS

Figure 8. Normalized numerical attenuation propagation velocity surfaces $\frac{v_i}{v}$ of the five-point scheme (3) and the average-derivative optimal nine-point scheme (2) for different propagation angles. In each plot, both $\frac{1}{G_i}$ and $\frac{1}{G_r}$ vary. Here $\frac{\Delta x}{\Delta z} = 2$.
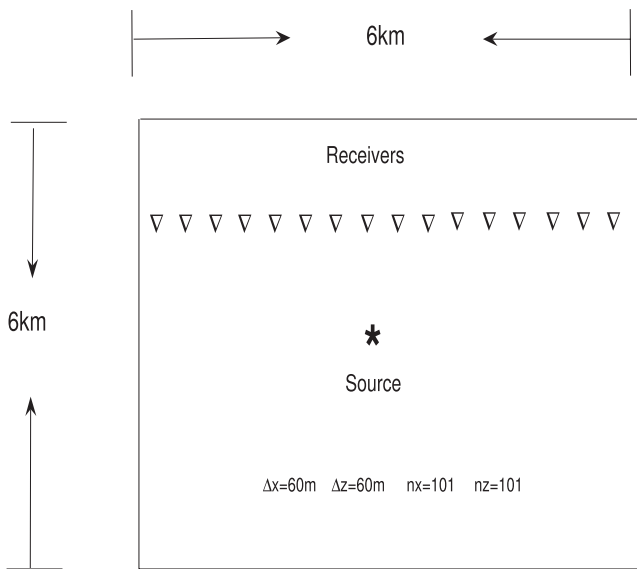

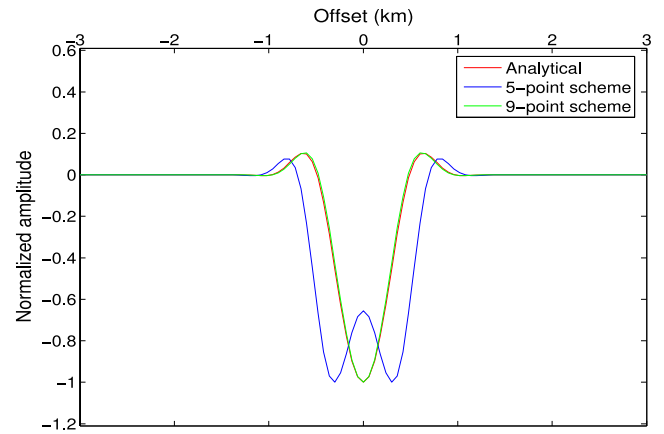**Figure 9.** Schematic of the homogeneous model.

Figure 10. Laplace-Fourier-domain seismograms computed with the analytical formula (15), the classical five-point scheme (3) and the average-derivative optimal nine-point scheme (2). Here $\frac{\Delta x}{\Delta z} = 1$.
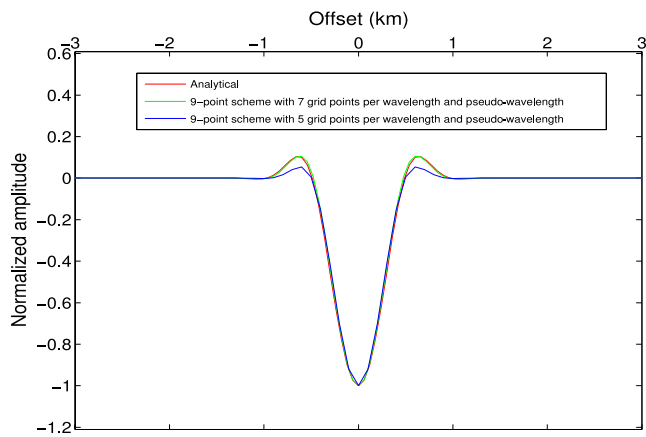
Figure 11. Laplace-Fourier-domain seismograms computed with the analytical formula (15), the average-derivative optimal nine-point scheme (3) with seven gridpoints per wavelength and pseudo-wavelength, and the average-derivative optimal nine-point scheme (3) with five gridpoints per wavelength and pseudo-wavelength. Here $\frac{\Delta x}{\Delta z} = 1$.
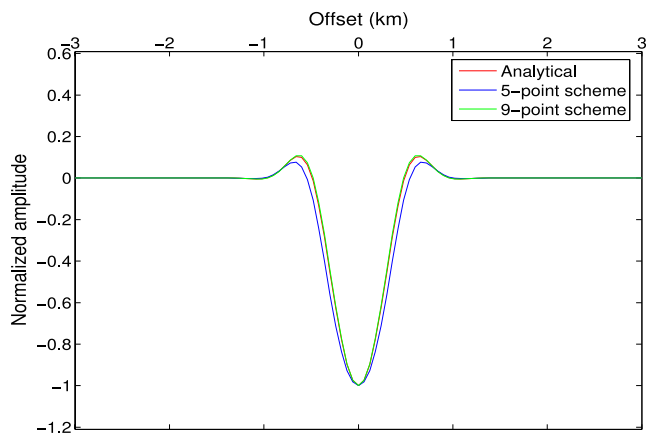

Figure 12. Laplace-Fourier-domain seismograms computed with the analytical formula (15), the classical five-point scheme (3) and the average-derivative optimal nine-point scheme (2). Here $\frac{\Delta x}{\Delta z} = 2$.

REFERENCES

Alford, R.M., Kelly, K.R. & Boore, D.M., 1974. Accuracy of finite-difference modeling of the acoustic wave equation, *Geophysics,* **39**(6), 834–842.

Brenders, A.J. & Pratt, R.G., 2007. Full waveform tomography for lithospheric imaging: results from a blind test in a realistic crustal model, *Geophys. J. Int.,* **168,** 133–151.

Chen, J.-B., 2012. An average-derivative optimal scheme for frequency-domain scalar wave equation, *Geophysics,* **77**(6), T201–T210.

Chen, J.-B., 2013. A generalized optimal 9-point scheme for frequency-domain scalar wave equation, *J. appl. Geophys.,* **92,** 1–7.
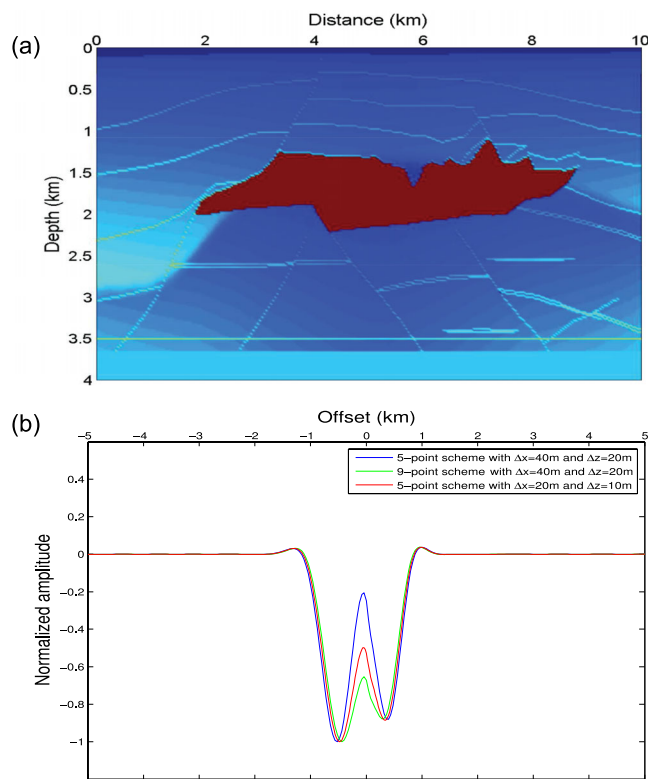
Figure 13. (a) The salt model. (b) Laplace-Fourier-domain seismograms computed with the classical five-point scheme (3) with $\Delta x = 40\,\text{m}$ and $\Delta z = 20\,\text{m}$, the average-derivative optimal nine-point scheme (2) with $\Delta x = 40\,\text{m}$ and $\Delta z = 20\,\text{m}$, and the classical five-point scheme (3) with $\Delta x = 20\,\text{m}$ and $\Delta z = 10\,\text{m}$.

Chen, J.-B., 2014. Dispersion analysis of an average-derivative optimal scheme for Laplace-domain scalar wave equation, *Geophysics,* **79**(2), T37–T42.

Ha, W. & Shin, C., 2012. Laplace-domain full-waveform inversion of seismic data lacking low-frequency information, *Geophysics,* **77**(5), R199–R206.

Ha, W., Chung, W., Park, E. & Shin, C., 2012. 2-D acoustic Laplace-domain waveform inversion of marine field data, *Geophys. J. Int.,* **190,** 421–428.

Jo, C.-H., Shin, C. & Suh, J.H., 1996. An optimal 9-point, finite-difference, frequency-space, 2-D scalar wave extrapolator, *Geophysics,* **61,** 529–537.

Pratt, R.G. & Worthington, M.H., 1990. Inverse theory applied to multi-source cross-hole tomography, part I: scalar wave-equation method, *Geophys. Prospect.,* **38,** 287–310.

Shin, C. & Cha, Y.H., 2008. Waveform inversion in the Laplace domain, *Geophys. J. Int.,* **173,** 922–931.

Shin, C. & Cha, Y.H., 2009. Waveform inversion in the Laplace-Fourier domain, *Geophys. J. Int.,* **177,** 1067–1079.

Shin, C., Cha, Y.H. & Park, K.P., 2010. Sequentially ordered single-frequency 2-D acoustic waveform inversion in the Laplace-Fourier domain, *Geophys. J. Int.,* **181,** 935–950.

Um, E.S., Commer, M. & Newman, G.A., 2012, Iterative finite-difference solution analysis of acoustic wave equation in the Laplace-Fourier domain, *Geophysics,* **77**(2), T29–T36.